1 **Title: Electrical Conductivity Studies on Silica Phases and the effects of Phase**

2 **Transformation**

3 **Running Title:** Electrical Conductivity on Silica Phases + Phase Transform

4 **Version:** Revision 1

5 **Date:** 29/07/2019

6

7 George M. Amulele[1,2], Anthony W. Lanati[1]*, and Simon M. Clark[1]

8 [1]

9   Australian Research Council Centre of Excellence for Core to Crust Fluid Systems

10 (CCFS)/GEMOC,

11 Department of Earth and Planetary Sciences,

12 Macquarie University

13 Balaclava Road, North Ryde

14 NSW, 2109, Sydney, Australia

15 [2]Present Address:

16 Earth, Environmental and Planetary Sciences

17 Case Western Reserve University

18 10900 Euclid Avenue, OH 44106

19 U. S. A.

20

21 *: Corresponding author

22

23

24 Keywords:

25 Electrical conductivity; Impedance Spectroscopy; Single crystal; Quartz; Silica;

26 Coesite; High-pressure.

1

Abstract

Starting with the same sample, the electrical conductivities of quartz, and coesite have been measured at pressures of 1, 6 and 8.7 GPa, respectively, over a temperature range of 373 – 1273K in a multi-anvil high-pressure system. Results indicate that the electrical conductivity in quartz increases with pressure as well as when the phase change from quartz to coesite occurs, while the activation enthalpy decreases with increasing pressure. Activation enthalpies of 0.89 eV, 0.56 eV and 0.46 eV, were determined at 1, 6, and 8.7 GPa, respectively, giving an activation volume of -0.052 ± 0.006 $cm^3\ mol^{-1}$. FTIR and composition analysis indicate that the electrical conductivities in silica polymorphs is controlled by substitution of silicon by aluminum with hydrogen charge compensation. Comparing with electrical conductivity measurements in stishovite, reported by Yoshino et al. (2014), our results fall within the aluminum and water content extremes measured in stishovite at 12 GPa. The resulting electrical conductivity model is mapped over the magnetotelluric profile obtained through the tectonically stable Northern Australian Craton. Given their relative abundances, these results imply potentially high electrical conductivities in the crust and mantle from contributions of silica polymorphs.

Key Points

- The electrical conductivity of silica polymorphs are determined by impedance spectroscopy up to 8.7 GPa.

- The activation enthalpy decreases with increasing pressure indicating a negative activation volume across the silica polymorphs.

- The electrical conductivity results are consistent with measurements observed in stishovite at 12 GPa.

2

52 **Introduction**

53   The mineral silica, SiO_2, occurs naturally as a constituent in many igneous and

54   sedimentary rocks. Silica exists in three major phases in the Earth. Firstly, as alpha

55   and beta quartz at pressures below 3-4 GPa with a transition temperature at about

56   550°C, secondly as coesite at pressures above 3-4 GPa and transition temperature

57   around 400-750°C, and thirdly as stishovite at pressures above 8-9 GPa with transition

58   temperatures around 750-1200°C. The crystal structures of these phases change from

59   hexagonal (quartz) to monoclinic (coesite) and finally to tetragonal (stishovite).

60   Silicon in quartz and coesite has a coordination number of four with oxygen at the

61   tetrahedral corners and this changes to six in stishovite. The relative abundance of all

62   three phases at the respective depths in the Earth is high and all have different

63   physical properties. A recent study has shown SiO_2 to crystallize from cooling of a Fe

64   – Si – O alloy, indicating the presence of stishovite on top of the Earth's outer core

65   (Hirose et al., 2017). Silica is also known to be able to incorporate other elements,

66   which contribute significantly to its physical properties. (Griggs and Blacic, 1965;

67   Holyoke and Kronenberg, 2013; Kronenberg et al., 1986; Stipp et al., 2006), and

68   many references therein, have discussed hydrolytic weakening in quartz as a result of

69   the uptake of water while Renner et al. (2001) have carried out similar studies on

70   coesite. With the incorporation of aluminum in its structure, stishovite can hold

71   substantial amounts of water, as a hydroxyl ion (Panero, 2006; Panero and Stixrude,

72   2004), contributing significantly to its physical and chemical properties. It is

73   important, therefore, to study the role of silica in mantle properties and dynamics

74   from the measurement of the electrical conductivities of its polymorphs and determine

75   how they relate to each other.

76 The substitution of silicon with aluminum and an alkali metal or hydrogen is

77 understood to contribute significantly to the electrical conductivity in silica. Studies

78 of the electrical conductivity in quartz have been carried out both in polycrystalline

79 aggregate (Bagdassarov and Delepine, 2004) as well as in single crystal (Wang et al.,

80 2014) quartz. The electrical conductivity in stishovite (Yoshino et al., 2014) has also

81 been recently reported. To our knowledge, no data on the electrical conductivity of

82 coesite at high pressures and temperatures has been reported.

83 In order to understand the electrical conductivity properties in the major

84 phases of silica and how they relate to each other it is important to study the

85 substitution mechanisms of Si for Al (plus an alkali or hydrogen ion) and how these

86 may affect the physical and chemical properties of the individual phases. With the

87 increase in pressure, it could be argued, that the mobility of an alkali ion or hydrogen

88 about the interstitial sites would be more difficult hence causing a decrease in

89 electrical conductivity. Studies on olivine, for example, show a modest reduction of

90 electrical conductivity with increase in pressure (Dai and Karato, 2014). Here we

91 report on the electrical conductivity in quartz and coesite at high pressures and show

92 that the electrical conductivity in quartz increases with pressure while the activation

93 enthalpy decreases, suggesting a negative activation volume. A further increase in the

94 electrical conductivity and decrease in the activation enthalpy is observed upon phase

95 transformation from quartz to coesite.

96

97 **Experimental Details**

98 Figure 1 shows the pressure-temperature cell assembly configuration used in

99 the conductivity measurements. Quartz powder, 99.9% purity, from Sigma-Aldrich

100 was loaded and compressed in an alumina cylinder then closed at both ends with

4

101   nickel disks. The nickel disks served as electrodes in the electrical conductivity

102   measurements as well as provided an oxygen buffer in the experiments. Two Pt/Pt-

103   10%Rh thermocouples were connected at both ends to the electrodes. These served to

104   measure temperature as well as complete the electrical conductivity path through the

105   sample. Heating was achieved by using a graphite furnace. 18 mm truncated edge

106   length (TEL) MgO-Cr_2O_3 doped octahedra were used and were compressed within a

107   cavity formed by 8, 11 mm TEL tungsten carbide (Toshiba Grade F) anvils using a

108   500-ton multi-anvil high-pressure press housed within Macquarie University High-

109   Pressure Laboratory. At least two temperature cycles were carried out in each

110   experiment, with temperatures held for minimal time during impedance spectra data

111   collection, at high temperatures so as to retain any structural water in the samples. In

112   order to avoid excessive cell moisture the starting powder and all ceramic

113   components, with the exception of the graphite heater, were stored in an oven at 393

114   K prior to assembly. Post-assembly the completed experimental cells were again

115   stored at 393 K for a minimum of 10 hours prior to loading in the press.

116

117   Three separate experiments were carried out at pressures of 1, 6 and 8.7 GPa, each

118   run made over a temperature range of 373 – 1273 K, with experiments held at 573K

119   following the first temperature decrease. A 1260 Solatron Impedance Gain-Phase

120   Analyzer was used to collect impedance spectra over a frequency range of 10 Hz - 1

121   MHz at increasing and decreasing temperatures. The electrical conductivity of the

122   sample at each temperature was then calculated using the expression:

123    $$\sigma = \frac{L}{Z' \cdot S} \tag{1}$$

124   where σ is the electrical conductivity, L and S is the length and the cross-sectional

125   area of the sample, respectively, and Z' is the real part of the electrical impedance.

5

126   The dimensions of the samples were measured on quenched samples, after the

127   experimental runs. The samples were sectioned and polished to the mid sections and

128   measurements carried out using a calibrated 2010 Leica M205C high resolution

129   optical microscope. The electrical conductivity relation with temperature at each

130   pressure was then determined using the Arrhenius relation:

131    $$\sigma = Ae^{\left(-\frac{\Delta H}{RT}\right)}$$ (2)

132   where A is the pre-exponent factor, ΔH the activation enthalpy, R the ideal gas

133   constant, and T is the temperature. Raman spectra were collected after each

134   experiment to verify the phases of the minerals present. A Horiba LABRAM HR

135   Evolution confocal laser Raman microscope was used for this analysis. The samples

136   were then polished down to a thickness of ~200μm and unpolarized FTIR

137   measurements carried out in transmission mode to determine the water contents. The

138   FTIR spectra were collected using a ThermoFisher iN10 FTIR spectrometer with

139   spectra collected over a frequency range of 3000- 4000 cm^{-1} using a 4 cm^{-1} resolution

140   and averaged over 128 scans. EPMA measurements were also carried out on the run

141   products using a Cameca SX100 probe to determine the sample compositions.

142

143   **Results**

144   Table 1 contains a summary of the experiments carried out and results

145   obtained. Experiments MQ016 and MQ011 were carried out at 1 and 6 GPa,

146   respectively. Figure 2 shows complex impedance spectrums at selected temperatures

147   from experiment MQ038, carried out at 8.7 GPa. Inductance was observed on the first

148   temperature increase, however, was absent on the first decrease in temperature and

149   subsequent cycles suggesting that any moisture within the experimental assembly was

150   driven off and, that the NiO solid state buffer actively buffering (S. Figure 1 and 2)

6

151 (Wang and Karato, 2013). Figure 3 shows a summary of the Arrhenius results from

152 the three experiments together with two results of stishovite obtained from Yoshino et

153 al. (2014). Raman analysis at the end of the experiments confirms the samples from

154 experiments MQ016 and MQ011 to be quartz, while that from experiment MQ038 to

155 be coesite (Figure 4).

156

157 Figure 5 shows the results from the FTIR analysis carried out on the samples after the

158 electrical conductivity experiments. For comparison and water content calculation

159 purposes, the amplitudes are plotted in absorption coefficient (cm^{-1}) indicating that

160 individual spectra are normalized to the thickness of that sample. FTIR analysis of

161 sample MQ016 shows a broad peak centered at 3400cm^{-1}. This characteristic broad

162 peak is similar to that observed in most feldspars (Johnson and Rossman, 2003; Yang,

163 2012). In quartz (Kronenberg, 1994) identifies this to be that from liquid water. One

164 other possible explanation is that it might be due to multiple OH sites. FTIR spectra

165 from MQ011, at higher pressure, shows more defined sharp peaks, evident of

166 structural water, even though it was also obtained from quartz. This implies that

167 structural water incorporation in quartz is only at higher pressures, hence having a

168 direct influence on the electrical conductivity. We use the IR results from Campone

169 et al. (1995) to label the peaks from MQ011. The peak at 3378cm^{-1} is identified as the

170 AlO$_4$-H stretching vibration (e$_2$ band) and peaks at 3428, 3478, and 3594 cm^{-1} as OH

171 stretching vibrations (s$_2$, s$_3$ and s$_4$ bands). The FTIR spectra measured on MQ038

172 shows the characteristic FTIR peaks of coesite. Peaks are observed at 3457, 3523 and

173 3600 cm^{-1} over a broad band centered at 3400 cm^{-1}, indicating that both intrinsic and

174 liquid water are present in the sample.

175   Beer-Lambert's law was used to calculate the water contents in the recovered

176   samples using the expression:

177
$$C_w = \int_{3000}^{3700} \frac{H(v)}{I \cdot t \cdot \gamma} dv \qquad (3)$$

178   where $\int H(v)\, dv$ is the absorption per cm integrated over the frequency range 3000 –

179   3700 cm^{-1}, I is the specific absorption coefficient of coesite obtained from Koch-

180   Muller et al. (2001) (190,000 l mol^{-1} cm^{-2}), t is the thickness of the sample and γ is the

181   orientation factor (0.5). The water contents calculated in the samples are shown in

182   Table 1.

183

184   Figure 3 shows the Arrhenius relation results of electrical conductivity changes in the

185   three experiments as a function of temperature. Two results from Yoshino et al.

186   (2014) on stishovite are plotted over our data for comparison. The activation enthalpy

187   of coesite at 8.7 GPa is comparable to that of nominally hydrous stishovite at 12 GPa.

188   There is an increase in electrical conductivity and a decrease in the activation

189   enthalpy associated with increase in pressure in quartz, as well as when quartz

190   transforms to coesite. The difference in electrical conductivity in quartz at low

191   temperatures is up to two orders of magnitude but then reduces and becomes

192   comparable at high temperatures. An order in magnitude increase of electrical

193   conductivity, however, is observed with the phase transformation from quartz to

194   coesite. Data from each experiment was fitted to the more general Arrhenius equation:

195
$$\sigma = AC_w^r e^{\left(-\frac{\Delta H}{RT}\right)} \qquad (4)$$

196   where r is the water content exponent. The fitted results are shown in Table 1.

197

198   **Discussion**

8

199 It is important to separate the effect of liquid (molecular) water and structural

200 (intrinsic) water on the electrical conductivity in minerals. The FTIR data of quartz

201 shown in Figure 5a) and b) suggest that water is incorporated in quartz as liquid water

202 at 1 GPa and as structural water at 6 GPa, respectively. This has also been

203 predominantly observed in natural undeformed samples of quartz (Kronenberg et al.,

204 2017). The peaks at 3310, 3378, and 3428 cm^{-1} indicate H$^+$ charge compensation for

205 Al^{3+} in Si^{4+} sites (Figure 5b) (Aines and Rossman, 1984). Experiments MQ016 and

206 MQ011 suggest that electrical conductivity increases with increasing pressure, while

207 activation enthalpy reduces with increasing pressure, implying a negative activation

208 volume in the mineral. The negative activation volume observed in quartz implies a

209 hopping conduction mechanism in the mineral (Goddat et al., 1999).

210

211 In experiment MQ038, carried out at 8.7 GPa, coesite shows both liquid and structural

212 water from the FTIR measurement, with a modest increase in the total water content

213 from the quartz experiment at 6 GPa. Koch-Muller et al. (2001) report that hydrogen

214 is only incorporated in the coesite structure at pressures above 5 GPa and 1100°C

215 temperature. In further work they conclude that the hydrogen solubility increases with

216 pressure and temperature (Koch-Muller et al., 2003). Unlike structurally incorporated

217 water, most molecular water would be depleted from a mineral at high temperatures,

218 hence having a direct effect on the electrical conductivity. There is a further decrease

219 in activation enthalpy with pressure from that reported in quartz at 6 GPa. Figure 6

220 shows the relation of activation enthalpy with pressure in quartz and coesite from the

221 three experiments carried out. A mean activation volume of -0.052 ± 0.006 cm^3 mol^{-1}

222 is calculated from the three experiments. This value is in contrast with that obtained

223 by (Wang et al., 2010), who determined an activation volume of 0.59 ± 0.14 cm^3 mol$^-$

224 [1] for quartz. Their value was determined from experiments carried out over the small

225 pressure range of 1 – 3 GPa which would be expected to give a large error.

226 Importantly, it is widely accepted (see Ito, 2007; and references therein) that multi-

227 anvil apparatus' not associated with light sources have effective pressure errors of at

228 least ± 0.5 GPa (Dai and Karato, 2009), dependent on calibration, below 10GPa and

229 double that above 10 GPa (Frost et al., 2004). This would therefore place the

230 experiments carried out at 1, 2, and 3 GPa within experimental error of one another.

231 Furthermore, a positive activation volume would also imply a decrease in electrical

232 conductivity with increasing pressure, which is not the case in our experiments,

233 carried out over a much larger range of pressure.

234

235 Within a mineral, the electrical conductivity is expected to decrease with pressure. A

236 reduction in the atomic spacing would result in smaller saddle spacing between atoms

237 for hopping to occur interstitially, thus decreasing the electrical conductivity and

238 increasing the activation enthalpy with pressure. This would imply a positive

239 activation volume. Bagdassarov and Delepine (2004), nonetheless, observe a slight

240 decrease in electrical conductivity with pressure in quartz over a pressure range of 0.5

241 – 2.0 GPa that they conducted measurements. The result we observed in quartz is the

242 opposite. We therefore conclude that with increasing pressure, the alkali to alkali or

243 hydrogen to hydrogen ions distances is decreased, and this increases the hopping

244 probability for an alkali or hydrogen ion to jump from one interstitial site to the next.

245 Goddat et al. (1999) refers to this as an increase in the exchange integral with increase

246 in pressure.

247

248 **Earth implications**

10

249   Quartz, and its associated polymorphs, are most prevalent within the crust and mantle

250   regions of the Earth, whilst being some of the most poorly covered with respect to

251   electrical conductivity studies. Within these regions, magnetotellurics has been used

252   to image both shallow and deep structures and features (Kühn et al., 2014; Selway,

253   2014; Selway et al., 2019) and references therein. The silica electrical conductivity

254   model presented in this study can be useful in monitoring of volcanic systems

255   (Aizawa et al., 2014; Aizawa et al., 2009; Aizawa et al., 2005; Díaz et al., 2012;

256   Ingham et al., 2009); in understanding shallow structures such as crustal scale brittle

257   and ductile fracture zones (Karas et al., 2017; Ozaydin et al., 2018; Tank et al., 2018);

258   in understanding deep earth structure and plumbing systems (Bai et al., 2010; Kühn et

259   al., 2014; Unsworth, 2010; Wannamaker et al., 2009); in searching for resource zones

260   (Cherevatova et al., 2015; Heinson et al., 2006); as well as in (volatile sensitive) deep

261   earth soundings studies (Adetunji et al., 2015; Cherevatova et al., 2015; Selway,

262   2014). Our investigations show that, for the same composition, quartz has the lowest

263   value of electrical conductivity among the three silica polymorphs of quartz, coesite

264   and stishovite. Figure 7 contextualizes this by comparing the electrical conductivity –

265   depth profiles carried out on quartz and coesite in our investigations with two other

266   investigations. These are values from single crystal measurements on quartz along

267   and perpendicular to the c-axis, carried out by Wang et al. (2010), as well as

268   magnetotelluric survey measurements of the Northern Australian lithosphere

269   (Heinson and White, 2005). The geotherm model suggested by Cull (1989) was used

270   to calculate the electrical conductivity depth profiles. At depths equivalent to 1 GPa

271   (~30 km), the electrical conductivity of quartz, in our measurements, is of the same

272   order as that obtained perpendicular to the c-axis in Wang et al. (2010) measurements,

273   that is in the order of $10^{-4.5}$ S/m. At much larger depths, and as water gets

274   incorporated into the structures of the high-pressure polymorphs of silica, the

275   electrical conductivity increases by about an order of magnitude, placing the electrical

276   conductivity values of all three polymorphs of silica well within the $10^{-3.5} - 10^{-2}$ S/m

277   range. This would have a significant effect on the electrical conductivities of mineral

278   aggregates that contain large proportions of silica in them.

279   In summary this work undertook several high-pressure electrical conductivity

280   experiments utilizing on quartz and coesite at several pressures over a temperature

281   range of 373K – 1273K generated from the same stating material. Electrical

282   conductivity is found to increase with pressure while the activation enthalpy decreases

283   with pressure. A negative activation volume value of -0.052 ± 0.006 cm^3 mol^{-1} is

284   calculated, confirming a hopping conductivity mechanism in silica polymorphs. Like

285   in stishovite, the electrical conductivities in quartz and silica is dependent on alumina

286   and water content. The contributions of quartz, coesite and stishovite to the overall

287   electrical conductivities of minerals in the Earth is significant given the proportion of

288   the respective mineral. Combined with studies by Yoshino et al. (2014) on stishovite,

289   this study provides useful results that can be used to model transport properties of

290   silica polymorphs in the Earth's crust and mantle.

291

292   **Acknowledgments**

12

311

312   **Author Contributions:**

313   GA designed the study in consultation with SMC. GA and AWL undertook all

314   experiments. GA undertook all analysis and interpretation of results in collaboration

315   with AWL. GA wrote the initial manuscript. AWL undertook extensive edits and

316   submitted the paper. All authors have contributed to, read, and agreed the final

317   manuscript.

13

References

318

319 Adetunji, A.Q., Ferguson, I.J., and Jones, A.G. (2015). Imaging the mantle

320 lithosphere of the Precambrian Grenville Province: large-scale electrical resistivity

321 structures. Geophysical Journal International 201, 1040-1061.

322 Aines, R.D., and Rossman, G.R. (1984). Water in minerals? A peak in the infrared.

323 Journal of Geophysical Research: Solid Earth 89, 4059-4071.

324 Aizawa, K., Koyama, T., Hase, H., Uyeshima, M., Kanda, W., Utsugi, M.,

325 Yoshimura, R., Yamaya, Y., Hashimoto, T., Yamazaki, K.i., Komatsu, S., Watanabe,

326 A., Miyakawa, K., and Ogawa, Y. (2014). Three-dimensional resistivity structure and

327 magma plumbing system of the Kirishima Volcanoes as inferred from broadband

328 magnetotelluric data. Journal of Geophysical Research: Solid Earth 119, 198-215.

329 Aizawa, K., Ogawa, Y., and Ishido, T. (2009). Groundwater flow and hydrothermal

330 systems within volcanic edifices: Delineation by electric self-potential and

331 magnetotellurics. Journal of Geophysical Research: Solid Earth 114,

332 Aizawa, K., Yoshimura, R., Oshiman, N., Yamazaki, K., Uto, T., Ogawa, Y., Tank,

333 S.B., Kanda, W., Sakanaka, S., Furukawa, Y., Hashimoto, T., Uyeshima, M., Ogawa,

334 T., Shiozaki, I., and Hurst, A.W. (2005). Hydrothermal system beneath Mt. Fuji

335 volcano inferred from magnetotellurics and electric self-potential. Earth and Planetary

336 Science Letters 235, 343-355.

337 Bagdassarov, N.S., and Delepine, N. (2004). alpha-beta inversion in quartz from low

338 frequency electrical impedance spectroscopy. Journal of Physics and Chemistry of

339 Solids 65, 1517-1526.

340 Bai, D., Unsworth, M.J., Meju, M.A., Ma, X., Teng, J., Kong, X., Sun, Y., Sun, J.,

341 Wang, L., Jiang, C., Zhao, C., Xiao, P., and Liu, M. (2010). Crustal deformation of

14

342   the eastern Tibetan plateau revealed by magnetotelluric imaging. Nature Geoscience

343   3, 358-362.

344   Campone, P., Magliocco, M., Spinolo, G., and Vedda, A. (1995). Ionic transport in

345   crystalline SiO_2: The role of alkali-metal ions and hydrogen impurities. Physical

346   Reveiw B 52, 15903-15908.

347   Cherevatova, M., Smirnov, M.Y., Jones, A.G., Pedersen, L.B., Becken, M., Biolik,

348   M., Cherevatova, M., Ebbing, J., Gradmann, S., Gurk, M., Hübert, J., Jones, A.G.,

349   Junge, A., Kamm, J., Korja, T., Lahti, I., Löwer, A., Nittinger, C., Pedersen, L.B.,

350   Savvaidis, A., and Smirnov, M. (2015). Magnetotelluric array data analysis from

351   north-west Fennoscandia. Tectonophysics 653, 1-19.

352   Cull, J.P. (1989). Geothermal models and mantle rheology in Australia.

353   Tectonophysics 164, 107 - 115.

354   Dai, L. and Karato, S.-i. (2009). Electrical conductivity of pyrope-rich garnet at high

355   temperature and high pressure. Physics of the Earth and Planetary Interiors 176(1):

356   83-88.

357   Dai, L. and Karato, S.-i. (2009). Electrical conductivity of orthopyroxene:

358   Implications for the water content of the asthenosphere. Proceedings of the Japan

359   Academy, Series B 85(10): 466-475.

360   Dai, L.D., and Karato, S. (2014). The effect of pressure on the electrical conductivity

361   of olivine under the hydrogen-rich conditions. Physics of the Earth and Planetary

362   Interiors 232, 51-56.

363   Díaz, D., Brasse, H., and Ticona, F. (2012). Conductivity distribution beneath Lascar

364   volcano (Northern Chile) and the Puna, inferred from magnetotelluric data. Journal of

365   Volcanology and Geothermal Research 217–218, 21-29.

15

366 Frost, D. J., Poe, B. T., Trønnes, R. G., Liebske, C., Duba, A., and Rubie, D. C.

367 (2004). A new large-volume multianvil system. Physics of the Earth and Planetary

368 Interiors 143-144: 507-514.

369 Goddat, A., Peyronneau, J., and Poirier, J.P. (1999). Dependence on pressure of

370 conduction by hopping of small polarons in minerals of the Earth's lower mantle.

371 Physics and Chemistry of Minerals 27, 81-87.

372 Griggs, D.T., and Blacic, J.D. (1965). Anomalous Weakness of Synthetic Crystals.

373 Science 147, 292.

374 Heinson, G., and White, A. (2005). Electrical resistivity of the Northern Australian

375 lithosphere: Crustal anisotropy or mantle heterogeneity? Earth and Planetary Science

376 Letters 232, 157-170.

377 Heinson, G.S., Direen, N.G., and Gill, R.M. (2006). Magnetotelluric evidence for a

378 deep-crustal mineralizing system beneath the Olympic Dam iron oxide copper-gold

379 deposit, southern Australia. Geology 34, 573-576.

380 Hirose, K., Morard, G., Sinmyo, R., Umemoto, K., Hernlund, J., Helffrich, G., and

381 Labrosse, S. (2017). Crystallization of silicon dioxide and compositional evolution of

382 the Earth's core. Nature 543, 99-102.

383 Holyoke, C.W. and Kronenberg, A.K. (2013). Reversible water weakening of quartz.

384 Earth and Planetary Science Letters 374, 185-190.

385 Ingham, M.R., Bibby, H.M., Heise, W., Jones, K.A., Cairns, P., Dravitzki, S., Bennie,

386 S.L., Caldwell, T.G., and Ogawa, Y. (2009). A magnetotelluric study of Mount

387 Ruapehu volcano, New Zealand. Geophysical Journal International 179, 887-904.

388 Ito, E. (2007). 2.08 - Theory and Practice – Multianvil Cells and High-Pressure

389 Experimental Methods. Treatise on Geophysics. G. Schubert. Amsterdam, Elsevier:

390 197-230.

16

391   Johnson, E.A. and Rossman, G.R. (2003). The concentration and speciation of

392   hydrogen in feldspars using FTIR and H-1 MAS NMR spectroscopy. Am Mineral 88,

393   901-911.

394   Karas, M., Tank, S.B., and Ozaydin, S. (2017). Electrical conductivity of a locked

395   fault: investigation of the Ganos segment of the North Anatolian Fault using three-

396   dimensional magnetotellurics. Earth Planets Space 69.

397   Koch-Muller, M., Dera, P., Fei, Y.W., Reno, B., Sobolev, N., Hauri, E., and

398   Wysoczanski, R. (2003). OH- in synthetic and natural coesite. American Mineralogist

399   88, 1436-1445.

400   Koch-Muller, M., Fei, Y., Hauri, E., and Liu, Z. (2001). Location and quantitative

401   analysis of OH in coesite. Physics and Chemistry of Minerals 28, 693-705.

402   Kronenberg, A.K. (1994). Hydrogen Speciation and Chemical Weakening of Quartz.

403   Reveiws in Mineralogy 29, 123-176.

404   Kronenberg, A.K., Hasnor, F.B.H.A., Holyoke, C.W., Law, R.D., Liu, Z.X., and

405   Thomas, J.B. (2017). Synchrotron FTIR imaging of OH in quartz mylonites. Solid

406   Earth 8, 1025-1045.

407   Kronenberg, A.K., Kirby, S.H., Aines, R.D., and Rossman, G.R. (1986). Solubility

408   and Diffusional Uptake of Hydrogen in Quartz at High Water Pressures - Implications

409   for Hydrolytic Weakening. Journal of Geophysical Research - Solid Earth 91, 2723-

410   2744.

411   Kühn, C., Küster, J., and Brasse, H. (2014). Three-dimensional inversion of

412   magnetotelluric data from the Central Andean continental margin. Earth, Planets and

413   Space 66, 112.

17

414   Ozaydin, S., Tank, S.B., and Karas, M. (2018). Electrical resistivity structure at the

415   North-Central Turkey inferred from three-dimensional magnetotellurics. Earth Planets

416   Space 70.

417   Panero, W.R. (2006). Aluminum incorporation in stishovite. Geophysical Research

418   Letters 33.

419   Panero, W.R., Stixrude, L.P. (2004). Hydrogen incorporation in stishovite at high

420   pressure and symmetric hydrogen bonding in delta-AlOOH. Earth and Planetary

421   Science Letters 221, 421-431.

422   Renner, J., Stockhert, B., Zerbian, A., Roller, K., and Rummel, F. (2001). An

423   experimental study into the rheology of synthetic polycrystalline coesite aggregates. J

424   Journal of Geophysical Research - Solid Earth 106, 19411-19429.

425   Roberts, J. J. and Tyburczy, J. A. (1994). Frequency dependent electrical properties of

426   minerals and partial-melts. Surveys in Geophysics 15(2): 239-262.

427   Selway, K. (2014). On the Causes of Electrical Conductivity Anomalies in

428   Tectonically Stable Lithosphere. Surveys in Geophysics 35, 219-257.

429   Selway, K., O'Donnell, J. P., and Özaydin, S. (2019). Upper mantle melt distribution

430   from petrologically constrained magnetotellurics. Geochemistry, Geophysics,

431   Geosystems, 20. https://doi.org/10.1029/2019GC008227

432   Stipp, M., Tullis, J., and Behrens, H. (2006). Effect of water on the dislocation creep

433   microstructure and flow stress of quartz and implications for the recrystallized grain

434   size piezometer. Journal of Geophysical Research - Solid Earth 111.

435   Tank, S.B., Ozaydin, S., and Karas, M. (2018). Revealing the electrical properties of a

436   gneiss dome using three-dimensional magnetotellurics: Burial and exhumation cycles

437   associated with faulting in Central Anatolia, Turkey. Physics of the Earth and

438   Planetary Interiors 283, 26-37.

439   Unsworth, M. (2010). Magnetotelluric Studies of Active Continent–Continent

440   Collisions. Surveys in Geophysics 31, 137-161.

441   Wang, D.J., Li, H.P., Yi, L., Matsuzaki, T., and Yoshino, T. (2010). Anisotropy of

442   synthetic quartz electrical conductivity at high pressure and temperature. Journal of

443   Geophysical Research - Solid Earth 115.

444   Wang, D. and Karato, S.-i. (2013). Electrical conductivity of talc aggregates at

445   0.5 GPa: influence of dehydration. Physics and Chemistry of Minerals 40(1): 11-17.

446   Wang, D.J., Yu, Y.J., and Zhou, Y.S. (2014). Electrical conductivity anisotropy in

447   alkali feldspar at high temperature and pressure. High Pressure Res 34, 297-308.

448   Wannamaker, P.E., Caldwell, T.G., Jiracek, G.R., Maris, V., Hill, G.J., Ogawa, Y.,

449   Bibby, H.M., Bennie, S.L., and Heise, W. (2009). Fluid and deformation regime of an

450   advancing subduction system at Marlborough, New Zealand. Nature 460, 733-736.

451   Yang, X.Z. (2012). An experimental study of H solubility in feldspars: Effect of

452   composition, oxygen fugacity, temperature and pressure and implications for crustal

453   processes. Geochimica Cosmochimica Acta 97, 46-57.

454   Yoshino, T., Shimojuku, A., and Li, D.Y. (2014). Electrical conductivity of stishovite

455   as a function of water content. Physics of the Earth and Planetary Interiors 227, 48-54.

456

457   **Figure Captions:**

458   Figure 1: Schematic of the electrical conductivity high-pressure cell.

459   Figure 2: Complex impedance spectra collected at decreasing temperature in

460   experiment MQ038.

461   Figure 3: Arrhenius relationships obtained in experiments MQ011, MQ016 and

462   MQ038. Also shown are the aluminum and water contents in wt. % measured in the

463   samples by EPMA. Comparison is made with stishovite data obtained from Yoshino,

464   2014.

465   Figure 4: Raman spectra analysis of the different phases of silica obtained in

466   experiments MQ011, MQ016 and MQ038. The reference spectra are obtained from

467   RRUFF database (Coesite RRUFF ID: X050094; Quartz RRUFF ID: R040031)

468   Figure 5: Unpolarized FTIR spectra of the different phases of silica obtained in

469   experiments a) MQ016, b) MQ011 and, c) MQ038. H^+ charge compensation for Al^{3+}

470   in Si^{4+} can be seen by the occurrence of bands 3310 3378 and 3428 in b).

471   Figure 6: Activation energy as a function of pressure in quartz and coesite

472   Figure 7: Comparison of electrical conductivity - depth profiles between

473   laboratory (present study and (Wang et al., 2010)) and transverse electric (TE)

474   and transverse magnetic (TM) magnetotelluric field measurements of the crust

475   by (Heinson and White, 2005).

476

477   S. Figure 1: Complex impedance plot of MQ011 showing the change in spectral

478   response as a function of temperature. Note the change from the first increase in

479   temperature (Red, Green and Black curves) and, the first decrease (Pink and Blue

480   curves) showing a loss of the second arc at higher temperatures, which has previously

481   been interpreted as direct measurements of cell moisture and grain boundary (Roberts

482   and Tyburczy, 1994; Dai and Karato, 2009b). Importantly, the second arc at higher

483   temperatures could be interpreted as a charge transfer, blocking (Dai and Karato,

484   2009a; Dai and Karato, 2009b; Dai and Karato, 2014), however this is absent in our

485   data.

486   S. Figure 2: Complex impedance plot of MQ016 showing the change in spectral

487   response as a function of temperature. Negative impedance curves (inductance) is

488   commonly associated with the interaction of the current between the sample and

489   electrode prior to development of the solid state buffer (i.e. NiO, in this case) or

490   dehydration of hydrous phases when present (Wang and Karato, 2013). However

491   these hydrous phases are absent in this study, therefore indicating the NiO buffer was

492   active in our experiments after the first heating cycle.

493
494

21

495

496   *Table 1: Summary of experimental conditions and results obtained from experiments*

Exp.	Pressure (GPa)	Phase from Raman	Water content (ppm wt. H_2O)		ΔH (eV)	$Log_{10}A$	r	Electrodes
			Initial	Final				
MQ016	1.0	Quartz	Dry	3606	0.86 ± 0.01	-2.60	0.56	Ni-NiO
MQ011	6.0	Quartz	Dry	185	0.56 ± 0.04	-1.63	0.50	Ni-NiO
MQ038	8.7	Coesite	Dry	624	0.46 ± 0.01	-2.44	0.46	Ni-NiO

497
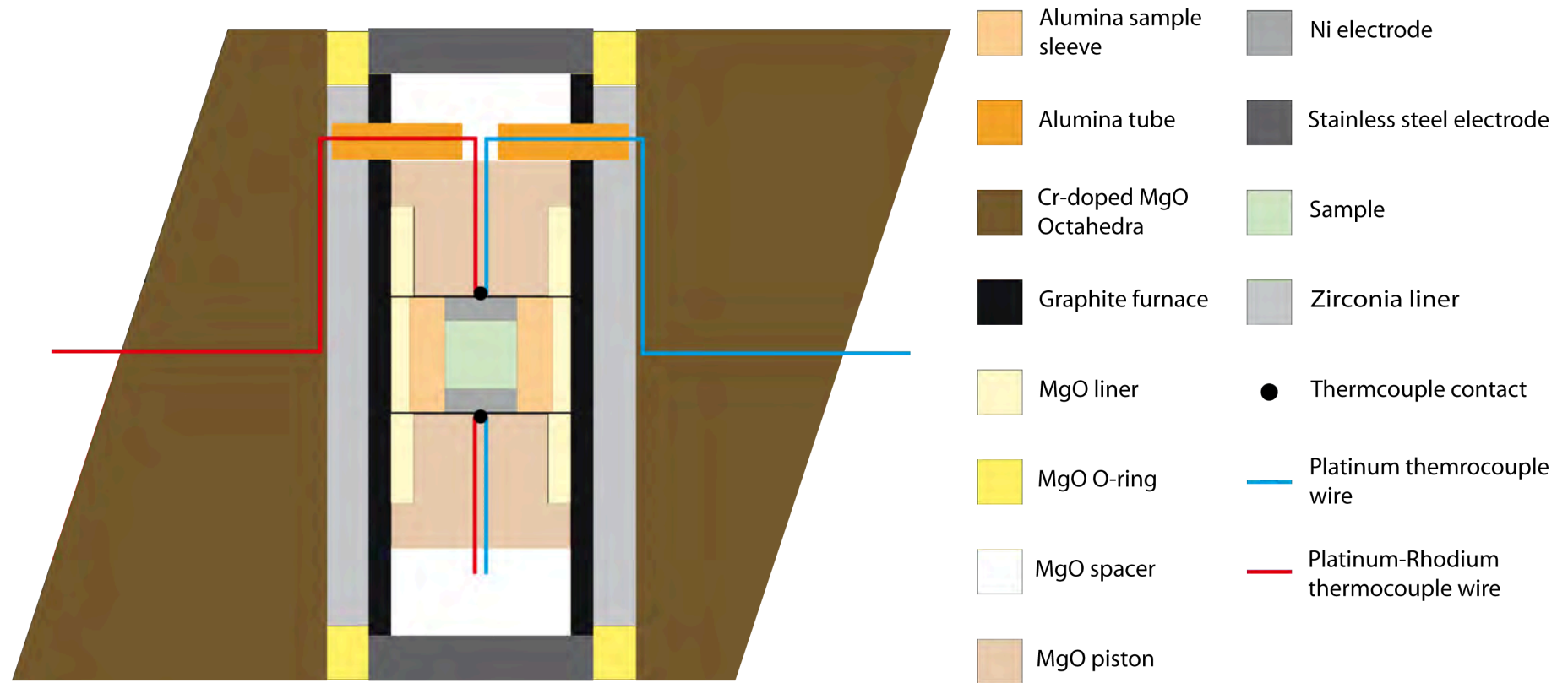
22

Figure 1: Schematic of the electrical conductivity high-pressure cell

498

499

23
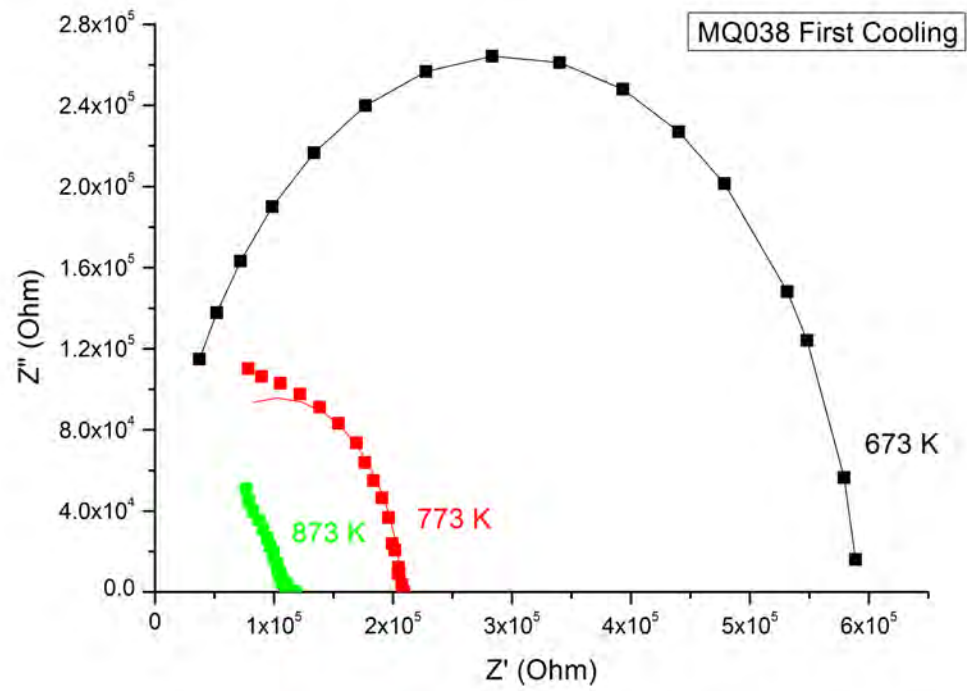
500

501   Figure 2: Complex impedance spectra collected at decreasing temperature in experiment MQ038
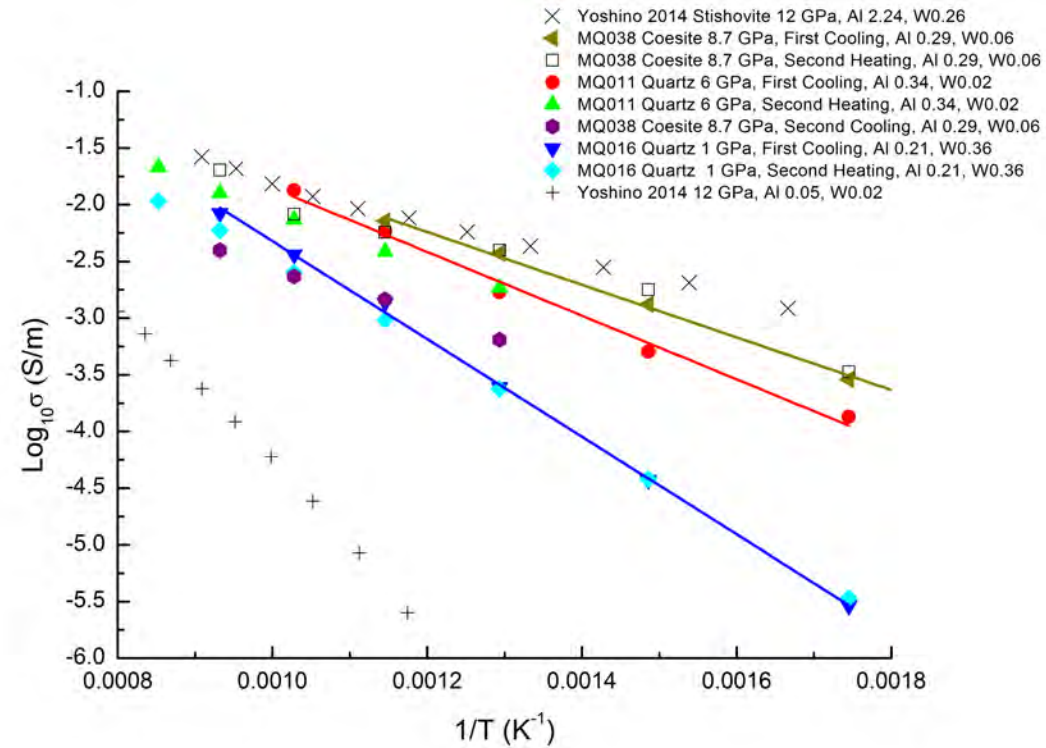
24

502

503

504   Figure 3: Arrhenius relationships obtained in experiments MQ011, MQ016 and MQ038. Also shown are the aluminum and water

505   contents in wt. % measured in the samples by EPMA. Comparison is made with stishovite data obtained from Yoshino et al. (2014).

506
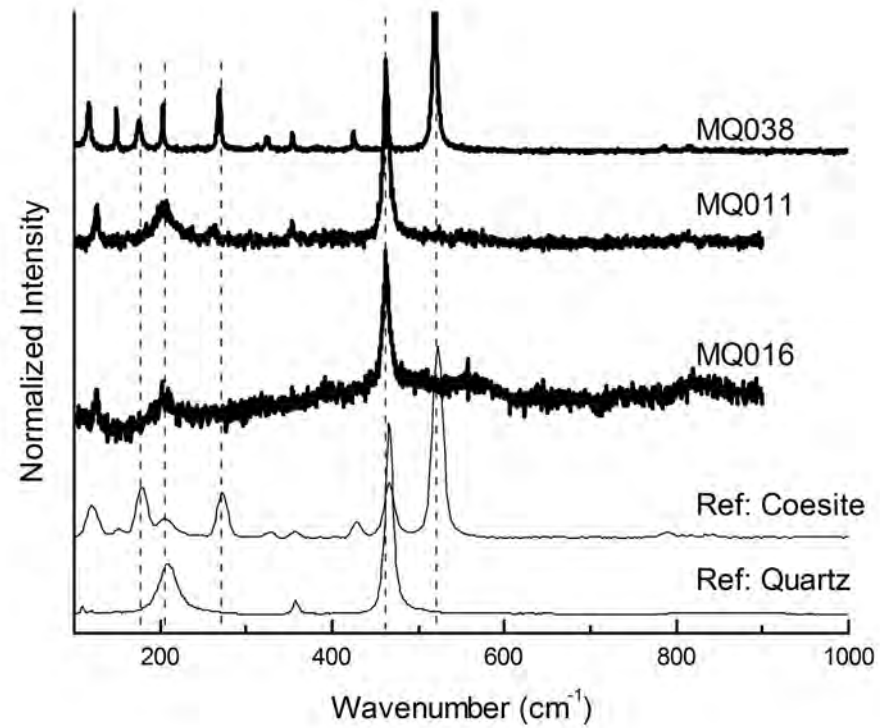
507

508

Figure 4: Raman spectra analysis of the different phases of silica obtained in experiments MQ011, MQ016 and MQ038.

The reference spectra are obtained from RRUFF database (Coesite RRUFF ID: X050094; Quartz RRUFF ID: R040031)
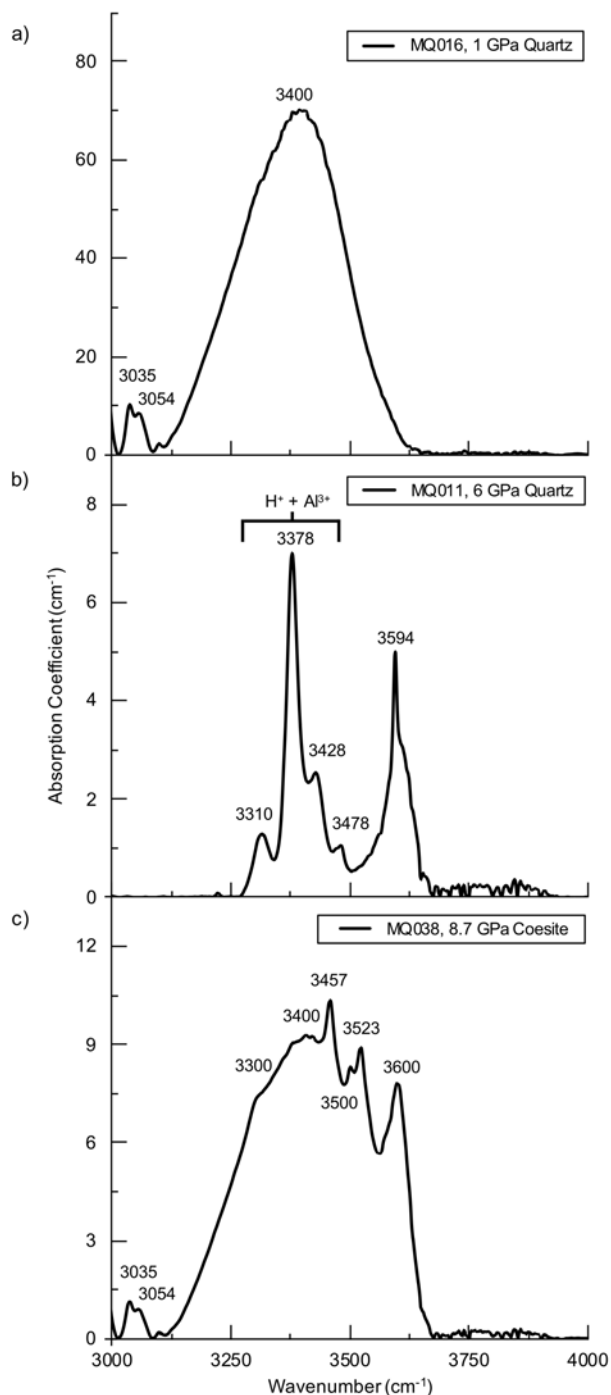
Figure 5: Unpolarized FTIR spectra of the different phases of silica obtained in experiments a) MQ016, b) MQ011 and, c) MQ038. H^+ charge compensation for Al^{3+} in Si^{4+} can be seen by the occurrence of bands 3310 3378 and 3428 in b).

27
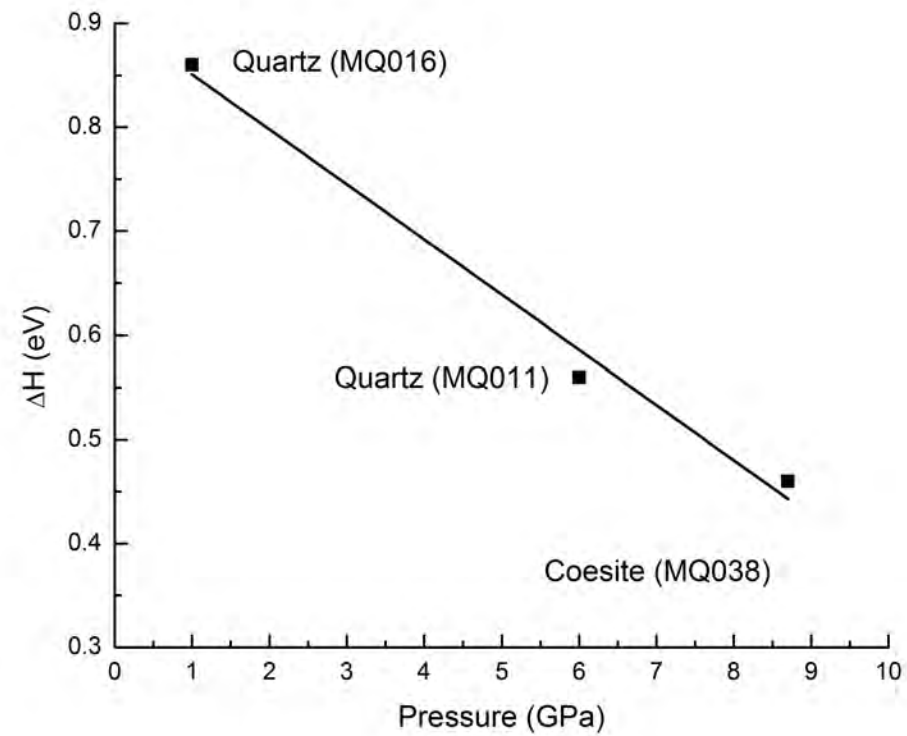
516

517   Figure 6: Activation energy as a function of pressure in quartz and coesite.

28

518
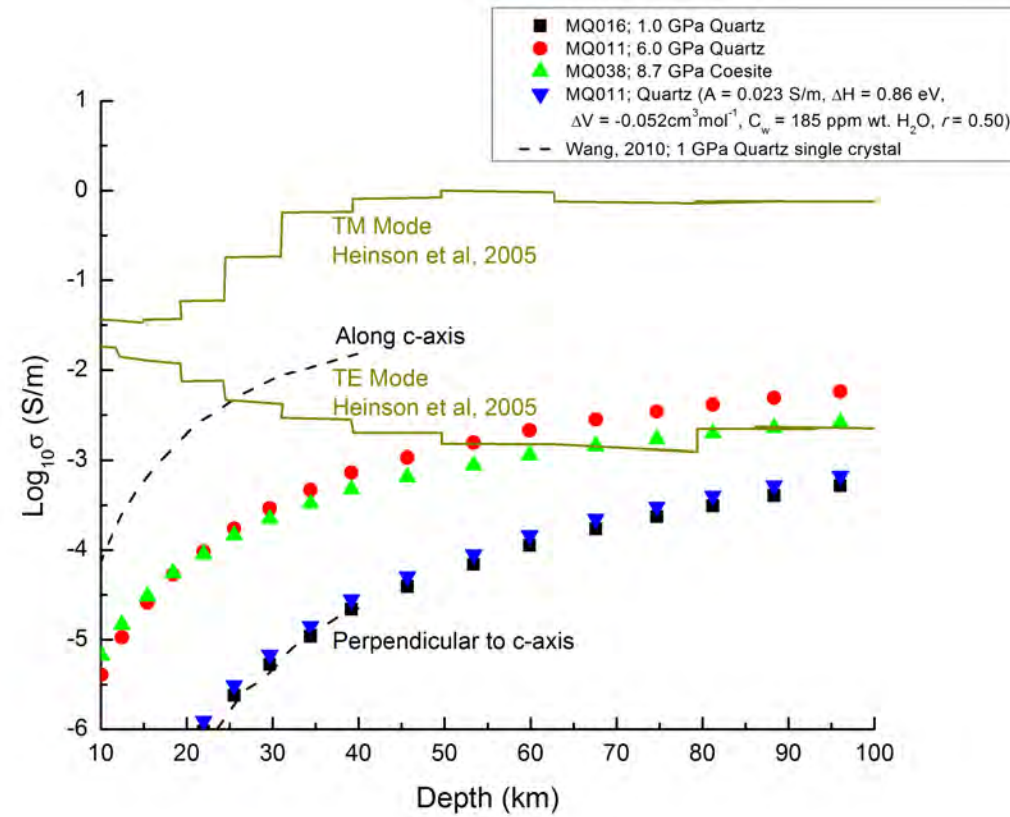
519

520   Figure 7: Comparison of electrical conductivity - depth profiles between laboratory (present study and (Wang et al., 2010)) and transverse

521   electric (TE) and transverse magnetic (TM) magnetotelluric field measurements of the crust by (Heinson and White, 2005).

522

29

523   **Supplementary Materials:**

524
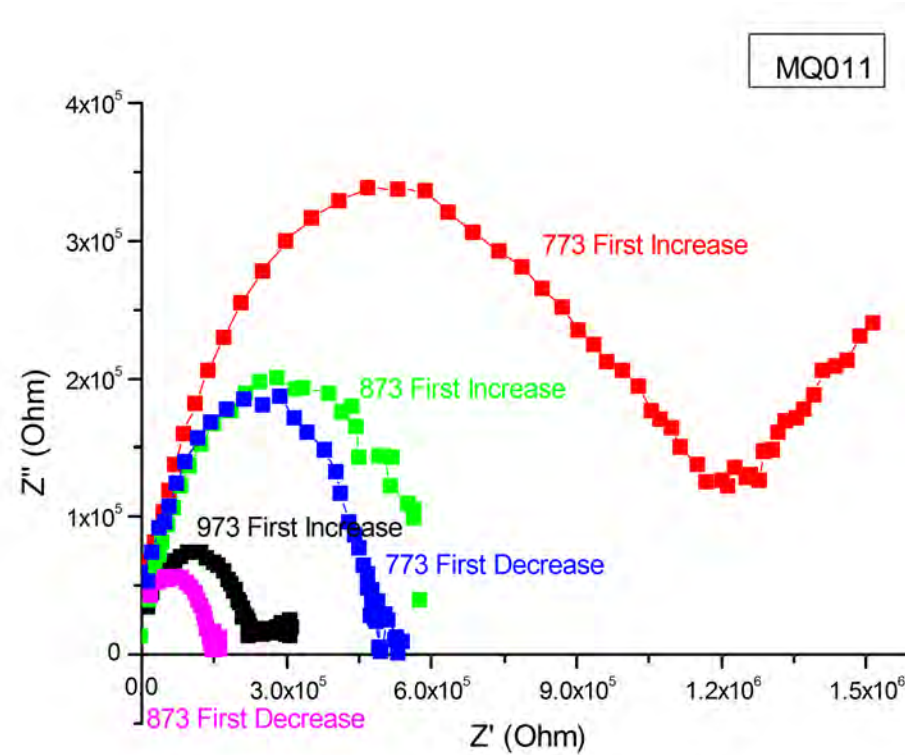
525

526   S. Figure 1: Complex impedance plot of MQ011 showing the change in spectral response as a function of temperature. Note the change from the

527   first increase in temperature (Red, Green and Black curves) and, the first decrease (Pink and Blue curves) showing a loss of the second arc at

30

528   higher temperatures, which has previously been interpreted as direct measurements of cell moisture and grain boundary (Roberts and Tyburczy,

529   1994; Dai and Karato, 2009b). Importantly, the second arc at higher temperatures could be interpreted as a charge transfer, blocking (Dai and

530   Karato, 2009a; Dai and Karato, 2009b; Dai and Karato, 2014), however this is absent in our data.

531
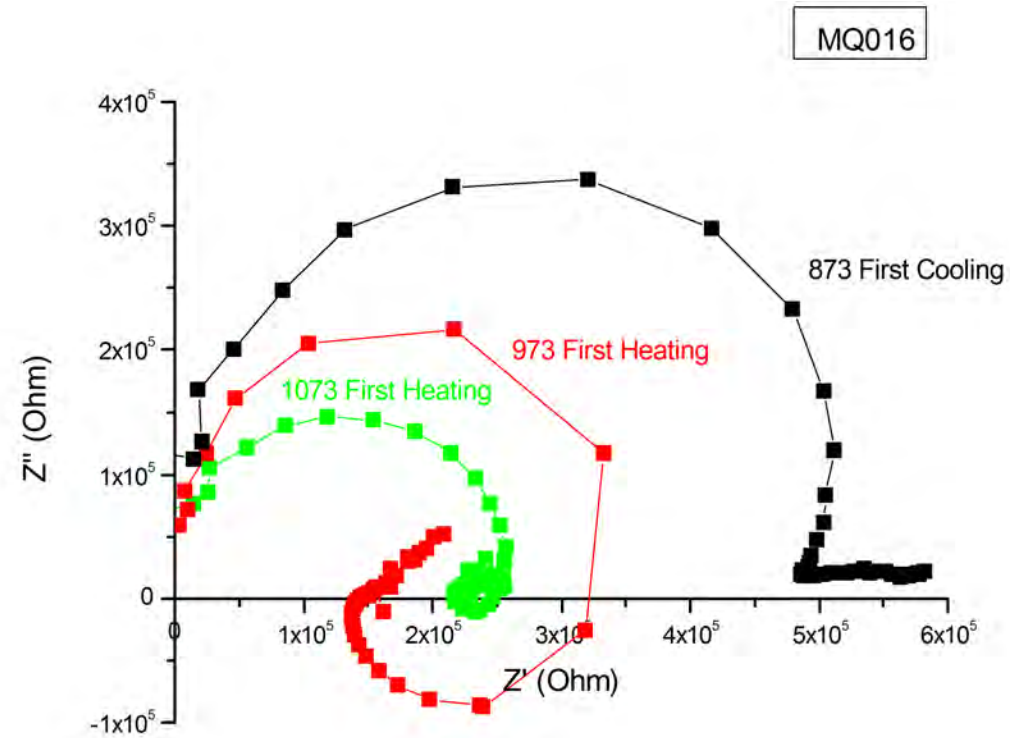
532

533   S. Figure 2: Complex impedance plot of MQ016 showing the change in spectral response as a function of temperature. Negative impedance

534   curves (inductance) is commonly associated with the interaction of the current between the sample and electrode prior to development of the

535   solid state buffer (i.e. NiO, in this case) or dehydration of hydrous phases when present (Wang and Karato, 2013). However these hydrous

536   phases are absent in this study, therefore indicating the NiO buffer was active in our experiments after the first heating cycle.

537

33